51st AIAA Aerospace Sciences Meeting including the New Horizons Forum and Aerospace Exposition
07 - 10 January 2013, Grapevine (Dallas/Ft. Worth Region), Texas

AIAA 2013-0422

Prediction of a Transonic Rotor Fluid/Structure Interaction With a Traveling Wave Using a Phase-lag Boundary Condition

Hong-Sik IM *, Ge-Cheng Zha†
Dept. of Mechanical and Aerospace Engineering
University of Miami
Coral Gables, Florida 33124
E-mail: gzha@miami.edu

Abstract

To use a sector of annulus for turbomachinery fluid/structure interaction (FSI) simulation, a time shifted phase lag (TSPL) is implemented at the circumferential boundaries where a phase lag condition exits based on a certain number of nodal diameters. A traveling wave initial condition to trigger the phase difference in blade vibration is also developed. For validation and comparison purpose for the phase-lag boundary conditions, full annulus flutter simulations of NASA Rotor 67 with backward traveling wave (BTW) of nodal diameter (N_D) of 1 and 2 are conducted using a fully coupled FSI methodology, in which time accurate Reynolds averaged 3D Navier-Stokes equations are solved with a system of 5-decoupled structure modal equations in a fully coupled manner. The predicted blade vibration behavior from the single passage FSI using the TSPL shows good agreement with the full annulus FSI simulation. The traveling wave initial condition captures very well the effect of the phase angle difference for turbomachinery FSI simulation in the present study.

Nomenclature

d	distance from the closest wall
e	total energy per unit mass
J	Jacobian of the coordinate transformation
I	identity matrix
L_∞	blade chord at hub
$\mathbf{l}$	normal vector on ξ surface with its magnitude equal to the elemental surface area and pointing to the direction of increasing ξ
l_t	grid moving velocity
N_B	total number of blades
N_{Bmesh}	number of blades used in the computational mesh
N_D	nodal diameter
Pr	Prandtl number
Pr_r	turbulent Prandtl number
q_k	total heat flux in Cartesian coordinates
R_e	Reynolds number, $\frac{\rho_\infty U_\infty L_\infty}{\mu_\infty}$
R_o	Rossby number, $\frac{\Omega L_\infty}{U_\infty}$
T	dimensionless period of phase lag based on nodal diameter and rotor speed, $\frac{2\pi}{R_o \times N_D}$
U, V, W	contravariant velocities in ξ, η, ζ direction
U_∞	reference velocity
y^+	dimensionless wall normal distance
δ_{ik}	Kronecker delta function

* Ph.D., AIAA Member
† Associate Professor, AIAA Associate Fellow

ν	kinematic viscosity
$\tilde{\nu}$	working variable of the S-A model related to turbulent eddy viscosity
Ω	rotor angular frequency in *radians/sec*, $\frac{2\pi \times RPM}{60}$
ϕ	geometry sector circumferential angle, $\frac{2\pi N_{Bmesh}}{N_B}$
φ	inter blade phase angle, $\frac{2\pi N_D}{N_B}$
τ_{ik}	shear stress in Cartesian coordinates

Subscripts

i, j, k	indices
∞	reference variable at free stream

Flutter parameters

b_s	bade root semi-chord
$\bar{m}$	blade mass
$\bar{V}$	frustum volume
V^*	reduced velocity, $\frac{U_\infty}{b_s \omega_\alpha}$
V_f	flutter speed index, $\frac{V^*}{\bar{\mu}}$
$\bar{\mu}$	mass ratio, $\frac{\bar{m}}{\bar{V}\rho_\infty}$
ω_α	1st torsional mode natural frequency
ω_j	blade natural frequency for jth mode
ζ_j	modal damping ratio for jth mode

1 Introduction

Robust and fast 3D tools for flutter prediction are key to success in the design of turbomachinery such as gas turbine engine fan/compressors. Flutter is an aeroelastic self-excited instability induced by fluid structure interaction of deformable structure with surrounding fluid flow. If vibration induced by aerodynamic force acting on the blade structure exceeds a condition of dynamic equilibrium, flutter of turbomachinery occurs, and often results in the blades failure.

For turbomachinery, flutter often involves traveling wave[1] in which the blades vibrate at the same frequency but with a constant phase difference termed as inter blade phase angle, IBPA(ϕ). The phase difference is defined as function of blade frequency(ω), nodal diameter(N_D) and number of blade (N_B).

For fluid-structural interaction simulation of a rotor flutter, it is not straightforward to automatically obtain the corresponding nodal diameter pattern[1, 2]. This is because the mass ratio($\bar{\mu}$) of turbomachinery blade is in general very large value, e.g. over 4000 for titanium alloy fan blades. It hence may require a very long CPU time to trigger a certain nodal diameter pattern, provided an appropriate circumferential perturbation is imposed as the inlet boundary condition.

In this paper, a traveling wave initial condition is implemented to start the blade vibration by a time lag based on IBPA. Note if the phase difference propagates in the same direction to the rotor rotation, it is called forward traveling wave(FTW). If the phase difference propagates in the opposite direction to the rotor rotation, it is called backward traveling wave(BTW). FTW or BTW is associated with N_D and usually observed during engine testing[3].

The phase-lag technique for circumferential boundary can significantly reduce the computational effort since it makes use of a reduced sector model instead of full annulus simulation. The phase-lag methods can be used as long as the phase shifted periodicity exits. When a single blade passage or a sector of the annulus is used for unsteady aerodynamic simulation, the effect of the phase difference needs to be considered due to the inter blade phase angle.

The numerical methods to treat phase angle difference at the circumferential boundaries have been proposed by several researchers[4, 5, 6, 7, 8]. The TSPL (time shifted phase lag) BC, known as the direct store method suggested by Erodes et al.[4], requires large computational memory since all flow variables are stored over a complete nodal diameter. Those stored data are then used to update the current solutions at the corresponding upper/lower periodic boundaries. Instead of using frequency information such as blade passing frequency or blade natural frequency, the time shifted conditions at the boundaries are determined based on the stored data for a nodal diameter cycle. With the direct store approach, no other assumption except for the phase-lagged condition itself is made.

A Fourier Series Phase lag BC, the so called shape correction method was proposed by He and Denton[5, 6].

The basic idea is to approximate the timewise variations of the flow variables in the Fourier series, and then store the Fourier components instead of the variables at each time step. Using these coefficients, the flow variables at the boundaries are regenerated. For most flow conditions of interest, the first few orders of Fourier coefficients are sufficient to predict the unsteady characteristics[5, 6, 7]. However, to use the He-Denton phase lag BC[5, 6] for complex turbomachinery aeromechanic problems such as non-synchronous, it is usually not obvious to give the frequency of the unsteady waves *a priori*. Because of this shortcoming, it is shown that the time shifted phase lag approach is more accurate in the prediction of flutter than the Fourier Series Phase lag. Srivastava et al.[7] compared the direct store method and the Fourier phase lag BC for a turbine cascade, and shows that once convergence is achieved, similar results are obtained. Overall, the TSPL BC is more general than the Fourier phase lag BC, but still limited to the temporal periodicity assumption, which does not exist when a rotating stall occurs.

Srivastava et al.[9] shows influence of shock wave on a transonic forward swept fan with supersonic tip using the energy method, in which the aerodynamic damping is used to determine flutter instability. With conventional energy method, aerodynamic damping is determined by the ratio of total blade work per one vibration cycle and time averaged kinetic energy[9]. If the blade vibration is underdamped, total blade work per one cycle will be positive and results in positive aerodynamic damping and no flutter. In other words, flutter occurs with negative aerodynamic damping. However, the energy method is shown to be inaccurate to capture the fan flutter boundary[2].

Vahdati et al.[10] uses a strongly coupled fluid/structure interaction to simulate a wide-chord transonic fan flutter. They indicate that the flow separation behind the shock on the suction surface is the key driver of the fan flutter. Chew et al.[11] used inviscid linearized model to capture stall flutter(or referred to as part-speed flutter) of a civil wide chord fan and a low aspect ratio military fan engine. Due to some shortcomings such as neglecting viscous terms, endwall boundary layers and tip clearance, their computation fails to show any signs of flutter instability, which was observed in the testing.

Gnesin et al.[12] solved the unsteady Euler equations with the modal approach for the structure analysis in the partially coupled manner. Doi et al.[13] loosely coupled an explicit Runge-Kutta multigrid flow solver with a FEM structure solver to predict the aeroelastic responses of NASA Rotor 67 blade. In the work of Carstens eta al.[14] and Sayma et al.[15], the structural part of the governing equations is time-integrated using Newmark scheme, while the unsteady airloads are computed at every time step by a Navier-Stokes code.

The main purpose of this study is to develop an accurate phase lag boundary condition for turbomachinery blade vibration with traveling waves. The TSPL is validated by using the NASA Rotor 67 full annulus flutter simulation with backward traveling wave at near peak efficiency condition.

To achieve accurate solutions of nonlinear fluid-structural interaction, the governing equations of structural and fluid motion have to be simultaneously solved. However, due to high CPU cost, many of fluid-structural interaction (FSI) simulations are implemented by a loosely coupled or non-fully coupled procedure[3, 16, 9, 2, 17, 18, 10, 11, 12, 13, 14, 15]. , i.e., the structural response lags behind the flow solver by one or a few time steps. The information is exchanged after partial or complete convergence of individual solvers[19].

The fully coupled FSI (fluid/structure interaction) approach[16, 20] is used to accurately predict interaction between flow and vibrating blades with an advanced moving mesh generation technique[16, 21] that can significantly reduce mesh skewness at the rotor tip clearance. Time accurate 3D compressible Navier-Stokes equations are solved with a system of 5-decoupled structure modal equations in a fully coupled manner. In order to decouple the equation of motion for the wing structure, transformation of the structural equations to the modal coordinates are applied. The flow field and structure always respond simultaneously by exchanging the unsteady aerodynamic force and structural deformation within each physical time step via a successive iteration on the pseudo-time step. The high-scalability parallel computing is applied to save wall clock time[22].

2 The Fluid Flow Model

Since there is shock/boundary layer interaction in the transonic NASA rotor 67 designed to have 22 blades and pressure ratio of 1.63 at design speed of 16043 rpm, the Low Diffusion E-CUSP (LDE) Scheme[23, 24] is used with the 3rd order MUSCL scheme for the inviscid flux and a 2nd order central differencing for the viscous flux. For turbulence closure, the Spalart-Allmaras (SA) model[25] is applied.

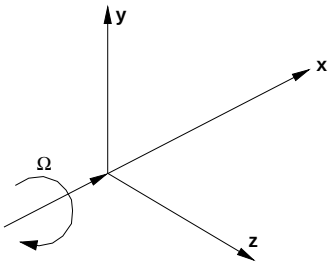

Figure 1: The Cartesian system rotating with angular velocity Ω around the x-axis

2.1 Navier-Stokes Equations in a Rotating Frame

The equation of motion of fluid flow for turbomachinery in a rotating frame of reference can be derived by adding the Coriolis force ($2\Omega\times\mathbf{V}$) and the centrifugal force($\Omega\times\Omega\times\mathbf{r}$) to the equation in the absolute frame. Expanding this momentum equation with continuity and energy equations in a rotating Cartesian system(x, y, z) as shown in Fig. 1 and applying coordinate transformation to the generalized coordinate system(ξ, η, ζ), the dimensionless Reynolds averaged 3D Navier-Stokes equations coupled with the SA model can be expressed as the following conservative form:

$$\frac{\partial \mathbf{Q}}{\partial t} + \frac{\partial \mathbf{E}}{\partial \xi} + \frac{\partial \mathbf{F}}{\partial \eta} + \frac{\partial \mathbf{G}}{\partial \zeta} = \frac{1}{Re}\left(\frac{\partial \mathbf{E}_v}{\partial \xi} + \frac{\partial \mathbf{F}_v}{\partial \eta} + \frac{\partial \mathbf{G}_v}{\partial \zeta} + \mathbf{S}\right) \tag{1}$$

where Re is the Reynolds number. The equations are nondimenisonalized based on airfoil chord L_∞, freestream density ρ_∞, velocity U_∞, and viscosity μ_∞. The conservative variable vector $\mathbf{Q}$, the inviscid flux vector $\mathbf{E}$, the viscous flux vector $\mathbf{E_v}$ and the source term vector $\mathbf{S}$ are expressed as follows and the rest can be expressed following the symmetric rule.

$$\mathbf{Q} = \frac{1}{J}\begin{pmatrix} \bar{\rho} \\ \bar{\rho}\tilde{u} \\ \bar{\rho}\tilde{v} \\ \bar{\rho}\tilde{w} \\ \bar{\rho}\tilde{e} \\ \rho\tilde{\nu} \end{pmatrix} \tag{2}$$

$$\mathbf{E} = \begin{pmatrix} \bar{\rho}U \\ \bar{\rho}\tilde{u}U + l_x\bar{p} \\ \bar{\rho}\tilde{v}U + l_y\bar{p} \\ \bar{\rho}\tilde{w}U + l_z\bar{p} \\ \left(\bar{\rho}\tilde{e} + \bar{p}\right)U - l_t\bar{p} \\ \rho\tilde{\nu}U \end{pmatrix} \tag{3}$$

$$\mathbf{E_v} = \begin{pmatrix} 0 \\ l_k\bar{\tau}_{xk} \\ l_k\bar{\tau}_{yk} \\ l_k\bar{\tau}_{zk} \\ l_k\left(\tilde{u}_i\bar{\tau}_{ki} - \bar{q}_k\right) \\ \frac{\bar{\rho}}{\sigma}\left(\nu + \tilde{\nu}\right)\left(\mathbf{l}\bullet\nabla\tilde{\nu}\right) \end{pmatrix} \tag{4}$$

$$\mathbf{S} = \frac{1}{J}\begin{pmatrix} 0 \\ 0 \\ \bar{\rho}{R_o}^2 y + 2\bar{\rho}R_eR_ow \\ \bar{\rho}{R_o}^2 z - 2\bar{\rho}R_eR_ov \\ 0 \\ \rho c_{b1}\left(1 - f_{t2}\right)\tilde{S}\tilde{\nu} + \frac{1}{Re}\left[-\rho\left(c_{w1}f_w - \frac{c_{b1}}{\kappa^2}f_{t2}\right)\left(\frac{\tilde{\nu}}{d}\right)^2\right. \\ \left. + \frac{\rho}{\sigma}c_{b2}\left(\nabla\tilde{\nu}\right)^2 - \frac{1}{\sigma}\left(\nu + \tilde{\nu}\right)\nabla\tilde{\nu}\bullet\nabla\rho\right] + Re\left[\rho f_{t1}\left(\Delta q\right)^2\right] \end{pmatrix} \tag{5}$$

where R_o is the Rossby number defined as $\frac{\Omega L_\infty}{U_\infty}$. ρ is the density, p is the static pressure, and e is the total energy per unit mass. The overbar denotes a regular filtered variable, and the tilde is used to denote the Favre filtered variable. ν is kinematic viscosity and $\tilde{\nu}$ is the working variable related to eddy viscosity in SA model. U, V and W are the contravariant velocities in ξ, η, ζ directions. For example, U is defined as follows.

$$U = l_t + \mathbf{l} \bullet \mathbf{V} = l_t + l_x\tilde{u} + l_y\tilde{v} + l_z\tilde{w} \tag{6}$$

$$l_t = \frac{\xi_t}{J}d\eta d\zeta, \qquad \mathbf{l} = \frac{\nabla\xi}{J}d\eta d\zeta \tag{7}$$

When the grid is stationary, $l_t = 0$. In the current discretization, $\Delta\xi = \Delta\eta = \Delta\zeta = 1$.

Let the subscripts i, j, k represent the coordinates x, y, z and use the Einstein summation convention. By introducing the concept of eddy viscosity to close the system of equations, the shear stress $\bar{\tau}_{ik}$ and total heat flux $\bar{q}_k$ in Cartesian coordinates can be expressed in tensor form as

$$\bar{\tau}_{ik} = (\mu + \mu_t)\left[\left(\frac{\partial\tilde{u}_i}{\partial x_k} + \frac{\partial\tilde{u}_k}{\partial x_i}\right) - \frac{2}{3}\delta_{ik}\frac{\partial\tilde{u}_j}{\partial x_j}\right] \tag{8}$$

$$\bar{q}_k = -\left(\frac{\mu}{Pr} + \frac{\mu_t}{Pr_t}\right)\frac{\partial\tilde{T}}{\partial x_k} \tag{9}$$

Above Eq.(8) and (9) are transformed to the generalized coordinate system in computation. The molecular viscosity $\mu = \mu(\tilde{T})$ is determined by Sutherland's law, and μ_t is determined by the SA model[25].

$$\mu_t = \bar{\rho}\tilde{\nu}f_{v1} \tag{10}$$

where

$$f_{v1} = \frac{\chi^3}{\chi^3 + c_{v1}^3}, \quad \chi = \frac{\tilde{\nu}}{\nu}$$

$$r = \frac{\tilde{\nu}}{R_e\tilde{S}k^2d^2}, \quad \tilde{S} = S + \frac{\tilde{\nu}}{R_ek^2d^2}f_{v2}, \quad f_{v2} = 1 - \frac{\chi}{1+\chi f_{v1}}$$

$$S = \sqrt{2\Omega_{ij}\Omega_{ij}}, \quad \Omega_{ij} = \frac{1}{2}\left(\frac{\partial u_i}{\partial x_j} - \frac{\partial u_j}{\partial x_i}\right)$$

The rest of auxiliary relations and the values of the coefficients given by reference[25] are used. The equation of state as a constitutive equation relating density to pressure and temperature is given as follows;

$$\bar{\rho}\tilde{e} = \frac{\bar{p}}{(\gamma - 1)} + \frac{1}{2}\bar{\rho}(\tilde{u}^2 + \tilde{v}^2 + \tilde{w}^2) - \frac{1}{2}\bar{\rho}r^2\Omega^2 \tag{11}$$

where $r(= \sqrt{y^2 + z^2})$ is the radius from the rotating axis, x. For simplicity, all the bar and tilde in above equations will be dropped in the rest of this paper.

2.2 Implicit Time Integration

The time dependent governing equation (1) is solved using dual time stepping method suggested by Jameson[26]. A pseudo temporal term $\frac{\partial Q}{\partial\tau}$ is added to the governing Eq. (1). This term vanishes at the end of each physical time step and has no influence on the accuracy of the solution. An implicit pseudo time marching scheme using line Gauss-Seidel line relaxation is employed to achieve high convergence rate instead of using an explicit scheme[27]. The pseudo temporal term is discretized with first order Euler scheme. Let m stand for the iteration index within a physical time step, the semi-discretized governing equation can be expressed as

$$\begin{aligned}\left[\left(\tfrac{1}{\Delta\tau} + \tfrac{1.5}{\Delta t}\right)I - \left(\tfrac{\partial R}{\partial \mathbf{Q}}\right)^{n+1,m}\right]\delta\mathbf{Q}^{\mathbf{n+1,m+1}} \\ = R^{n+1,m} - \tfrac{3\mathbf{Q}^{\mathbf{n+1,m}} - \mathbf{4Q^n} + \mathbf{Q^{n-1}}}{2\Delta t}\end{aligned} \tag{12}$$

where $\Delta\tau$ is the pseudo time step, and R is the net flux of the discretized Navier-Stokes equations evaluated at a grid point.

3 Structural Model

For the rotating blades in the relative frame of reference, on can assume that the stiffness of the rotor disk is much larger than that of the compressor blades, the vibration characteristics of the blades is dominant such that rotor disk vibration effect is negligible.

3.1 Modal Approach

The equation of motion of an N-DOF(degree of freedom) system with the mechanical damping and the aerodynamic loading as the excitation force can be presented in matrix form:

$$[\mathbf{M}]\{\ddot{\mathbf{X}}\} + [\mathbf{C}]\{\dot{\mathbf{X}}\} + [\mathbf{K}]\{\mathbf{X}\} = \{\mathbf{F}\} \tag{13}$$

where, **M**, **C**, **K** are the mass, structural damping and stiffness matrices. **F** is total aerodynamic force acting on the blade surface. It is demonstrated by Gruber and Carstens[28] that viscous effects can cause a significant difference in aerodynamic damping. Viscous force is included in total aerodynamic force i.e.

$$\mathbf{F} = -\oint P \cdot \hat{n} dA + \oint \tau_{\mathbf{w}} \cdot \hat{t} dA \tag{14}$$

where, $\hat{n}$ is the unit normal vector to the blade surface and $\hat{t}$ is the unit tangent vector to the blade surface. P is the fluid static pressure and $\tau_{\mathbf{w}}$ is the fluid wall shear stress acting on the blade surface. The effects of viscosity can not be neglected for the highly loaded transonic rotor because rotating stall with large structure of flow separation may occur in/near stall conditions.

To decouple the equations of motion for the damped systems(13), we use the mass normalized mode shape($\tilde{\phi}$) defined as the normal modes divided by square root of the the generalized mass($\sqrt{\phi^T m \phi}$). Let $\{\mathbf{X}\} = [\tilde{\Phi}]\{\mathbf{q}\}$ and premultiply Eq. (13) by the transpose $[\tilde{\Phi}]^T$.

$$\begin{aligned}[\tilde{\Phi}]^T[\mathbf{M}][\tilde{\Phi}]\{\ddot{\mathbf{q}}\} + [\tilde{\Phi}]^T[\mathbf{C}][\tilde{\Phi}]\{\dot{\mathbf{q}}\} + [\tilde{\Phi}]^T[\mathbf{K}][\tilde{\Phi}]\{\mathbf{q}\} \\ = [\tilde{\Phi}]^T\{\mathbf{F}\}\end{aligned} \tag{15}$$

where **q** is the vector of the principal coordinates. Using the orthogonality of the system matrices and assuming damping matrix to be a linear combination of the mass and stiffness matrices, Eq. (15) is then completely decoupled and the jth equation will have the form

$$\ddot{q}_j + 2\zeta_j \omega_j \dot{q}_j + \omega_j^2 q_j = \frac{\tilde{\phi}_j^T}{m_j}\mathbf{F} \tag{16}$$

where $[\tilde{\Phi}]^T = [\tilde{\phi}_1, \cdots, \tilde{\phi}, \cdots, \tilde{\phi}_N]^T$. N is the number of modal coordinates. ω_j and ζ_j are natural frequency and modal damping ratio for mode j. m_j denotes the jth diagonal element of modal mass matrix which will be unity. In the current study, the structural system may be reduced to only five mode shapes, since a few bending and torsional frequencies are usually sufficient to determine flutter. The normalized modal equation can be given as[20]

$$\ddot{q}_j + 2\zeta_j(\tfrac{\omega_j}{\omega_\alpha})\dot{q}_j + (\tfrac{\omega_j}{\omega_\alpha})^2 q_j = \frac{\tilde{\phi}_j^{*T}}{m_j^*} \cdot \mathbf{F}^* \cdot {V_f}^2 \cdot \frac{b_s^2 L_\infty}{\bar{V}} \cdot \bar{m} \tag{17}$$

where the dimensionless quantities are denoted by an asterisk. $V_f (= \frac{U_\infty}{b_s \omega_\alpha \sqrt{\bar{\mu}}})$ is the flutter speed index which is an input flutter control parameter. $\bar{m}$ is the measured blade mass, $\bar{V}$ represents the conical frustum volume and b_s is the streamwise root semi chord. L_∞ is the reference length and ω_α is the angular frequency of the first torsional mode in units *radians/sec*. $\bar{\mu} (= \frac{\bar{m}}{\bar{V}\rho_\infty})$ stands for the mass ratio, i.e. the ratio between the structural mass and the mass of the equivalent volume of fluid at reference density. It is noticed that m_j^* should be equal to one when the mass normalized mode shapes are used.

The equations are then transformed to a state form as follows:

$$[\mathbf{M}]\frac{\partial \mathbf{S}}{\partial t} + [\mathbf{K}]\{\mathbf{S}\} = \mathbf{q} \tag{18}$$

where

$$\mathbf{S} = \begin{pmatrix} q_j \\ \dot{q}_j \end{pmatrix}, \mathbf{M} = [I], \mathbf{K} = \begin{pmatrix} 0 & -1 \\ (\frac{\omega_j}{\omega_\alpha})^2 & 2\zeta_j(\frac{\omega_j}{\omega_\alpha}) \end{pmatrix}$$

$$\mathbf{q} = \begin{pmatrix} 0 \\ \phi_j^{*T} \cdot \mathbf{F}^* \cdot V_f \cdot \frac{b_s^2 L}{V} \cdot \bar{m} \end{pmatrix}$$

3.2 Implicit Structural Solver

To solve the structural equations with CFD solver[23, 24] in a fully coupled manner, the decoupled structural equations are integrated using the same method as the flow governing equations(12) within each physical time step:

$$\begin{aligned} &\left(\tfrac{1}{\Delta\tau} I + \tfrac{1.5}{\Delta t} M + K\right) \delta S^{n+1,m+1} \\ &= q^{n+1,m+1} - M \tfrac{3S^{n+1,m} - 4S^n + S^{n-1}}{2\Delta t} - K S^{n+1,m} \end{aligned} \tag{19}$$

The fully coupled procedure for fluid-structure interaction (FSI) simulation developed for 3D wing flutter[20], in which time lag between the fluid flow and the structure are removed, is implemented for turbomachinery as sketched in Fig.2. Within each physical time step(m), the flow and structural governing equations are solved without time lag via every successive pseudo time step until the net flux residual R given by Eq. (12) satisfies the prescribed convergence criteria(ε). Note the residual q for the structure equation (19) gets converged quickly within a few steps. Therefore, the convergence of FSI is determined according to R. After the convergence criteria is reached, the fluid-structural interaction goes to next physical time step, $n+1$.

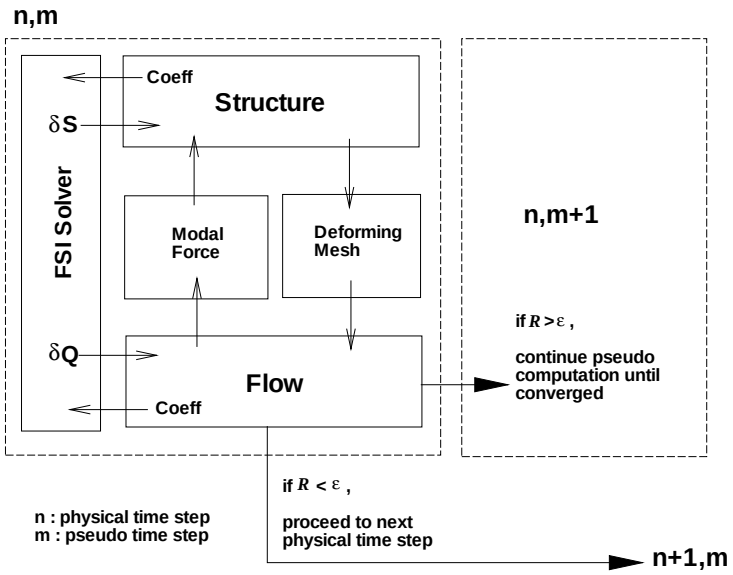

Figure 2: Procedure of fully coupled fluid-structure interaction

4 Deforming Mesh

A CPU efficient deforming mesh technique is one of the requisites for FSI to accurately describe the vibration of the structure. The conventional method regenerates mesh inside domain with the fixed outer boundaries. However this may cause significant numerical instability due to the high mesh skewness when the vibrating structure is close to the boundaries like rotor tip clearance. In this study an advanced deforming mesh algorithm proposed by the present authors[16, 21] is employed to improve mesh quality over rotor tip clearance.

5 Time Shifted Phase Lag BC

To avoid calculation of full annulus rotor, a boundary condition needs to be setup on the circumferential boundaries of a sector of the rotor where a phase difference exists due to the blade rotation. The time shifted phase lag (TSPL) BC, also called direct store phase lag BC, suggested by Erods et al.[4] and Srivastava et al.[7] based on phase periodicity with the period as one nodal diameter is applied. Since the present solver uses the ghost cell approach at boundaries as sketched in Fig.3, the Cell GL(ghost cell of the lower periodic boundary) corresponds to the cell IU(inner cell of the upper periodic boundary), and vice versa for the cell GU and the cell IL.

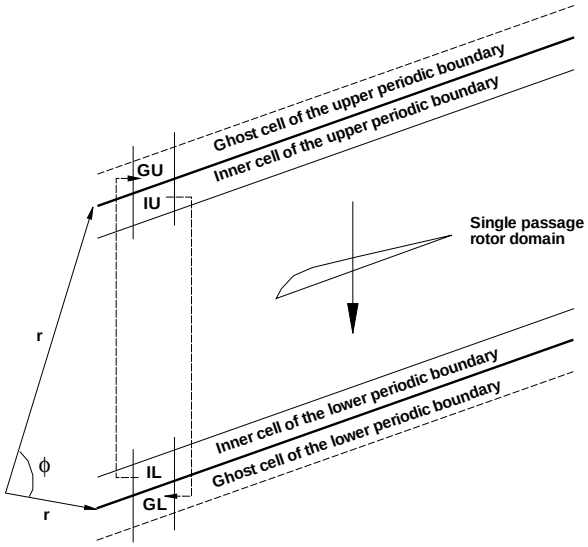

Figure 3: Sketch of Fourier phase lag domain

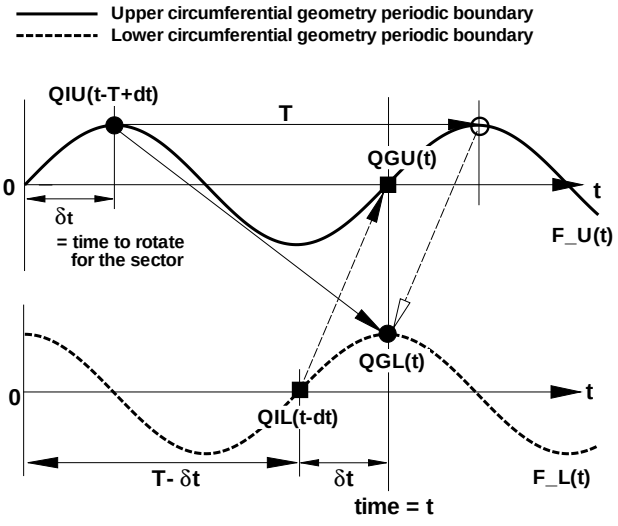

Figure 4: Sketch of the time shift phase lag BC

As sketched in Fig. 4, let us assume that the rotor rotates from the upper circumferential boundary to the lower circumferential boundary such that information at the upper side is delayed by time δt. T is the period of one nodal diameter (N_D). To update the upper/lower circumferential boundaries, first the conservative variables of the upper inner cells(Q_{IU}) and the lower inner cells(Q_{IL}) are stored for δt and $T - \delta t$ respectively. Then, these stored values

are rotated by the sector circumferential angle, ϕ to update boundary ghost cells. The upper ghost cell Q_{GU} at time t can be updated using Q_{IL} at time $T-\delta t$. However, the lower ghost cell Q_{GL} at time t can not be updated using the upper ghost cell values since Q_{IU} at time $t+\delta t$ is not available. The way to update Q_{GL} is to take one cycle-lagged value, Q_{IU} at time $T-t+\delta t$, by assuming phase periodicity as depicted in Fig. 4. Note that any frequency input is no longer needed for the present TSPL BC. The boundaries are treated as in-phase condition for the first cycle since the stored Q at both sides are not available.

$$Q_{GL}(t) = Q_{IU}(t+\delta t) = Q_{IU}(t-T+\delta t) \tag{20}$$

$$Q_{GU}(t) = Q_{IL}(t-\delta t) \tag{21}$$

where T is dimensionless period of phase lag based on one nodal diameter and rotor speed, and δt is dimensionless time taken by the rotor to rotate by the sector circumferential angle, ϕ. Note that δt is the same for any nodal diameter, but the period T decreases linearly as nodal diameter increases.

$$T = \frac{2\pi}{R_o \times N_D} \tag{22}$$

$$\delta t = \frac{\phi}{R_o} \tag{23}$$

6 Traveling Wave Initial Conditions

To trigger a traveling wave for the fully coupled FSI, a time lag technique that renders each blade mode to start vibrating by a time lag (Δt) is implemented. N_D must be given to define φ.

$$\Delta t_j = \frac{\varphi}{\omega_j} \tag{24}$$

where the subscript j denotes the blade vibration mode and

$$\varphi = \frac{2\pi N_D}{N_B} \tag{25}$$

The traveling wave is only implemented as initial condition. In other words, each blade is set to freely vibrate initially with a time lag determined by Eq. (24) and the vibration pattern is controlled by the fully coupled FSI solver after the initial condition. No any other perturbation or boundary condition is used to enforce the nodal diameter pattern after the initial condition.

7 Other Boundary Conditions

At the rotor inlet, the constant radial distributions of total pressure, total temperature, swirl angle and pitch angle are specified from the experiment[29]. Then, the components of velocity are extrapolated from the inner domain to determine the rest of variables[21]. At the rotor outlet, the back pressure is specified at the hub, and the blade spanwise distribution is then determined by solving the simplified radial equilibrium equation. The components of velocity are extrapolated from the computational domain. On the solid wall, the non-slip boundary condition is applied to enforce mass flux going through the wall to be zero. To avoid the fine mesh near the hub/casing wall, the law of the wall is applied[21]. The wall static pressure on the hub/casing is also determined by using the radial equilibrium equation in the generalized coordinate system[30]. In addition, the adiabatic condition is used to impose zero heat flux through the wall.

8 Computational Mesh for NASA Rotor 67

NASA rotor 67[29] with 22 blades is simulated in this study for its flutter behavior. The full annulus mesh generated using the H-O-H mesh topology is shown in Fig. 5. The mesh convergence test was done for three different mesh sizes via the previous rotating stall simulation by the present authors[31, 32]. The current mesh size showed a

good agreement with the experiment[29] for the rotor speed-line prediction. The single passage mesh has 121(around blade)×77(blade-to-blade)×49(span), and the full annulus mesh is then built by copying the single passage mesh. For a fully gridded tip model with nominal tip clearance, an O-block mesh of 121×12×9 is used. The mesh uses 9 points in the spanwise direction to resolve tip clearance flow. The 1st grid spacing on the the blade surface was set to $5 \times 10^{-}5$ times the blade hub chord length which gives $y^{+} < 3$, while on the hub and casing surface it was set to $2 \times 10{-}^{3}$ times blade hub chord which can give y+ around 50. Therefore, the wall function BCs[31, 32] are used on the hub and casing. Total 14 blocks per blade(308 blocks for full annulus) are used for the parallel computation.

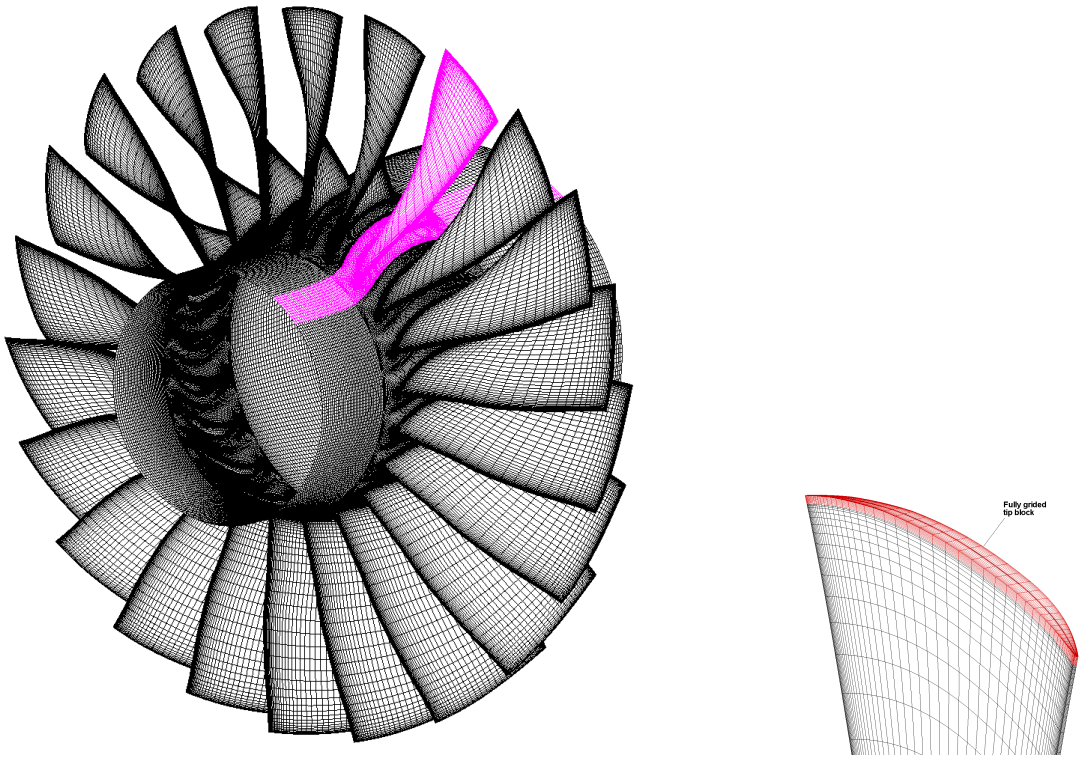

Figure 5: Computational mesh for full annulus NASA rotor 67

9 Mode Shape for NASA Rotor 67

For the present flutter simulation of NASA rotor 67, the first five mode shapes normalized by the generalized mass[16] are used. The rotor blades are assumed as titanium alloy properties with Young's modulus=1.172×10^{11} Pa, Poisson's ratio=0.3, and density 4539 kg/m^3 since the material properties used in original design has not been reported. The effect of centrifugal force is taken into account. The blades are modeled as fixed at the rigid body rotor. The grid data on the blade surface used in CFD mesh is imported for ABAQUS FE modeling. The first five natural frequencies of Rotor 67 is 584.04 Hz, 1474.9 Hz, 2017.5 hz, 3181.7 Hz, and 3789.9 Hz. RPM of NASA Rotor 67 at normal operating condition is 16043, which results in the blade passing frequency(BPF) of 5882.4 Hz.

10 Traveling Wave Simulation

Near peak efficiency condition is chosen for flutter simulations of NASA rotor 67 with a backward traveling wave for $N_D = 1$ and 2. The total-to-total pressure ratio is about 1.62 at near peak point and 100% speed is 16043 rpm. In the current study, a uniform structural damping ratio of 0.005 is used. To reduce computational efforts, the flow field was initialized using the steady state full annulus simulation. A dimensionless time step of 0.0017 is used. The unsteady flutter computation is started using the initialized flow field obtained by the steady CFD only. The residual in each physical time step is reduced by two orders of magnitude, which is achieved usually within 20 pseudo time iterations. The traveling wave initial condition is setup only using the first mode frequency based on Eq. (24).

The modal displacements with a backward traveling wave of $N_D = 1$ and 2 are presented in Fig. 6. For $N_D = 1$, one blade vibration cycle of the rotor full annulus is clearly captured while two cycles appear for $N_D = 2$. It is shown that the present traveling wave BC given in Eq. (24) simulates very well the phase angle difference in terms of N_D that travels in the opposite to the rotor rotation for all modes considered in this study (mode 4 and 5 are not shown here).

Fig. 7 shows 1st mode displacements and modal force ($\frac{\tilde{\phi}_1^{*T}}{m_1^*} \cdot \mathbf{F}^* \cdot {V_f}^2 \cdot \frac{b_s^2 L}{\bar{V}} \cdot \bar{m}$) of blade 1, 6 and 11 for $N_D = 1$ and 2. The rotor has no flutter at near peak condition since the blade responses are damped out. The phase difference of blades for $N_D = 1$ and 2, which appears at both displacements and force, increases with the backward traveling wave in the opposite direction to the rotor rotation since blade 1 is the starting point of wave propagation. The amplitude level of $N_D = 2$ is a little smaller than that of $N_D = 1$, which indicates that aerodynamic damping of $N_D = 2$ is larger than $N_D = 1$ since the blade vibration of $N_D = 2$ decays more quickly than $N_D = 1$. The work of Srivastava et al.[9] on a transonic fan flutter indicates that aerodynamic damping of the fan blade increases as IBPA increases with its peak at 180°.

11 Time Shifted Phase Lag BC Validation

In order to validate the time shifted phase lag BC, the single passage FSI simulations of NASA Rotor 67 are conducted using the time shifted phase lag BC. The inter blade blade phase angle(IBPA, $\varphi = N_D 2\pi / N_{blade}$) for the single passage flutter simulation is obtained by assuming $N_D = 1$ and 2.

Fig. 8 shows the normalized mass flux (ρU) at corresponding lower/upper ghost cell of the circumferential points. The phase angle differences are well captured by the single passage FSI simulation with the present TSPL for $N_D = 1$ and 2 based on the rotor frequency.

The 1st, 2nd and 3rd modal displacements for $N_D = 1$ and 2 predicted by the TSPL and the full annulus are presented in Fig. 9. The blade responses are damped out for all blade modes without flutter. Overall, the TSPL shows good agreement with the full annulus for both $N_D = 1$ and 2 in the 1st and 2nd blade mode. However, small difference appears in the 3rd mode, which is acceptable since amplitude of the 3rd mode is much smaller than that of the 1st mode. The 1st mode is dominant in the present blade flutter vibration.

Fig. 10 shows the 1st, 2nd and 3rd modal force ($\frac{\tilde{\phi}_j^{*T}}{m_j^*} \cdot \mathbf{F}^* \cdot {V_f}^2 \cdot \frac{b_s^2 L}{\bar{V}} \cdot \bar{m}$) for $N_D = 1$ and 2 predicted by the TSPL and the full annulus. There is a clear difference between the single passage simulations with the TSPL and the full annulus, which may be caused by the lack of blade interaction with the single passage simulation.

The tip leading edge (LE) deflections of blade 1 in θ-direction ($\tan^{-1}\frac{z_i}{y_i}$ - $\tan^{-1}\frac{z_o}{y_o}$) predicted by the single passage with the TSPL BC and the full annulus are plotted in Fig. 11. In the θ-direction deflection formulation, the subscript i represents instant physical time step and o denotes initial position of the blade tip LE. It is obvious that there is small difference of the blade responses between $ND = 1$ and 2 for the full annulus. The single passage simulations with the TSPL BC shows the same displacements between $ND = 1$ and 2 because it is difficult for a single passage blade with a phase lag BC to accurately capture the effect of blade interaction that plays a dominant role in turbomachinery flutter.

Time-averaged speed line at near peak efficiency point predicted by the full annulus and TSPL for $N_D = 1$ is shown in Fig. 12. The TSPL shows good agreement with the experiment[29] and the full annulus.

12 Conclusion

The time shift phase lag boundary condition (TSPL) is implemented to conduct single blade passage flutter simulations. In order to consider the effect of phase angle difference, a traveling wave initial condition is developed by implementing a time lag based on IBPA. The full annulus flutter simulations of NASA Rotor 67 with backward traveling wave of $N_D = 1$ and 2 are conducted at near peak efficiency condition using the fully coupled fluid/structure interaction. It is shown that the fully coupled flutter simulation using the traveling wave reflects very well the phase angle difference in the blade flutter. The single blade passage flutter simulations with the TSPL accurately predicts the blade vibration level and IBPA compared with the full annulus results. However, the single blade passage FSI simulation does not accurately capture the subtle effect of nodal diameter variation due to lacking the inter-blade flow interaction, whereas the full annulus FSI simulation resolves very well the effect of nodal diameter that causes a small difference in the aerodynamic damping and blade responses.

Acknowledgments

The grants support from AFRL and the industrial partners of GUIde Consortium 10-AFRL-1024 is acknowledged. The numerical simulations are conducted at the Center for Computational Sciences at the University of Miami and Air Force Research Lab DoD Supercomputing Resource Centers.

References

[1] F. Lane, "System Mode Shapes in the Flutter of Compressor Blade Rows," *Journal of the Aeronautical Science*, vol. 23, pp. 54–66, 1956.

[2] R. Srivastava, and T. S. R. Reddy, "Comparative Study of Coupled-Mode Flutter-Analysis Methods for Fan Configurations," *Journal of Propulsion and Power*, vol. 15, pp. 447–453, May-June 1999.

[3] A.J. Sanders, K.K. Hassan, and D.C. Rabe, "Experimental and Numerical Study of Stall Flutter in a Transonic Low-Aspect Ratio Fan Blisk," *Journal of Turbomachinery*, vol. 126, pp. 166–174, 2004.

[4] J.I. Erods, E. Alzner, and W. McNally, "Numerical Solution of Periodic Transonic Flow Through a Fan Stage," *AIAA Journal*, vol. 15, pp. 1559–68, Nov. 2004.

[5] L. He, and J.D. Denton, "Three-Dimensional Time Marching Inviscid and Viscous Solutions for Unsteady Flows Around Vibrating Blades," *Journal of Turbomachinery*, vol. 116, pp. 469–476, 1994.

[6] H. D. Li, and L. He, "Blade Aerodynamic Damping Varaition With Rotor-Stator Gap: A Computational Study Using Single-Passage Approach," *Journal of Turbomachinery*, vol. 127, pp. 573–578, Jul. 2005.

[7] R. Srivastava, M.A. bakhle, T.G. Keith Jr, and G.L. Stefko, "Aeroelastic Analysis of Turbomachinery: Part I-Phase Lagged Boundary Condition Methods," *International Journal of Numerical Methods for Heat & Fluid Flow*, vol. 14, pp. 366–381, Nov. 2004.

[8] S. Ji, and F. Liu, "Flutter Computation of Turbomachinery Cascades Using a Parallel Unsteady Navier-Stokes Code," *AIAA Journal*, vol. 37, pp. 320–327, 1999.

[9] R. Srivastava, and T.G. Keith Jr., "Influence of Shock Wave on Turbomachinery Blade Row Flutter," *Journal of Propulsion and Power*, vol. 21, pp. 167–174, 2005.

[10] M. Vahdati, G. Simpson, and M. Imregun, "Mechanisms for Wide-Chord Fan Blade Flutter," *Journal of Turbomachinery*, vol. 133, pp. 041029–1–041029–7, 2011.

[11] J.W. Chew, R.J. Hamby, J.G. Marshall, and M. Vahdati, " Part Speed Flutter of Transonic Fan." RTO AVT Symposium on Design Principles and Methods for Aircraft Gas Turbine Engines, Toulouse, France, May 1998, 1998.

[12] V. Gnesin, and R. Rzadkowski, "A Coupled Fluid-Structure Analysis for 3-D Inviscid Flutter of IV Standard Configuration," *Journal of Sound and Vibration*, vol. 251, pp. 315–327, 2002.

[13] H. Doi, and J.J. Alonso, "Fluid/Structure Coupled Aeroelastic Computations for Transonic Flows in Turbomachinery." GT2002-30313,Proceedings of ASME Turbo Expo 2002, 2002.

[14] V. Carstens, R. Kemme, and S. Schmitt, "Coupled Simulation of Flow-Structrue Interaction in Turbomachinery," *Aerospace Science and Technology*, vol. 7, pp. 298–306, June 2003.

[15] A.I. Sayma, M.V. Vahdati, and M. Imregun, "Turbine Forced Response Prediction Using an Integrated Non-Linear Analysis," *Proceedings of the Institution of Mechanical Engineers, Part K: Journal of Multi-body Dynamics*, vol. 214, pp. 45–60, 2000.

[16] H.-S. Im, X.-Y. Chen, and G.-C. Zha, " Detached Eddy Simulation of Transonic Rotor Stall Flutter Using a Fully Coupled Fluid-Structure Interaction." ASME GT2011-45437, ASME Turbo Expo 2011, Vancouver, Canada, June 2011, 2011.

[17] R. Srivastava, J. Panovsky, R. Kielb, L. Virgin, and K. Ekici, "Nonlinear Flutter in Fan Stator Vanes With Time Dependent Fixity," *Journal of Turbomachinery*, vol. 134, pp. 021009–1–021009–8, 2012.

[18] M. Vahdati, A.I. Sayma, C. Bread, and M. Imregun, "Computational Study of Intake Duct Effects on Fan Flutter Stability," *AIAA Journal*, vol. 40, pp. 408–418, 2002.

[19] R. Kamakoti, and W. Shyy, "Fluid-Structure Interaction for Aeroelastic Applications," *Progress in Aerospace Sciences*, vol. 40, pp. 535–558, 2004.

[20] X.Y. Chen, G.-C. Zha, M.-T. Yang, "Numerical Simulation of 3-D Wing Flutter with Fully Coupled Fluid-Structural Interaction," *Journal of Computers & Fluids*, vol. 36, pp. 856–867, 2007, doi:10.1016/j.compfluid.2006.08.005.

[21] H. Im, "High Fidelity Simulation of Non-Synchronous Vibration for Aircraft Engine Fan/Compressor." PhD Dissertation, University of Miami, 2012.

[22] B. Wang, Z. Hu, and G. Zha, "A General Sub-Domain Boundary Mapping Procedure For Structured Grid CFD Parallel Computation," *AIAA Journal of Aerospace Computing, Information, and Communication*, vol. 5, pp. 425–447, 2008.

[23] G.C. Zha, Y.Q. Shen, and B.Y. Wang, "An Improved Low Diffusion E-CUSP Upwind Scheme ," *Journal of Computer and Fluids*, vol. 48, pp. 214–220, 2011, doi:10.1016/j.compfluid.2011.03.012.

[24] Zha, G.C., Shen, Y.Q., and Wang, B.Y., "Calculation of Transonic Flows Using WENO Method with a Low Diffusion E-CUSP Upwind Scheme." AIAA Paper 2008-0745, 46th AIAA Aerospace Sciences Meeting, Reno, NV, Jan. 2008.

[25] P.R. Spalart, and S.R. Allmaras, "A One-equation Turbulence Model for Aerodynamic Flows." AIAA-92-0439, 1992.

[26] A. Jameson, "Time Dependent Calculations Using Multigrid with Applications to Unsteady Flows Past Airfoils and Wings." AIAA Paper 91-1596, 1991.

[27] Y.Q. Shen, B.Y. Wang, and G.C. Zha, "Implicit WENO Scheme and High Order Viscous Formulas for Compressible Flows ." AIAA Paper 2007-4431, 2007.

[28] B. Gruber, and V. Carstens, "The impact of Viscous Effects on the Aerodynamic Damping of Vibrating Transonic Compressor Blades - A Numerical Study," *Journal of Turbomachinery*, vol. 123, pp. 409–417, 2001.

[29] A.J. Strazisar, J.R. Wood, M.D. Hathaway, and K.L. Suder, "Laser Anemometer Measurements in a Transonic Axial-Flow Fan Rotor." NASA Technical Paper 2879, November, 1989.

[30] X.Y. Chen, H.S. Im, and G.C. Zha, "Fully Coupled Fluid-Structural Interaction of a Transonic Rotor at Near-Stall Conditions Using Detached Eddy Simulation." AIAA Paper 2011-228, Jan. 2011.

[31] H.S. Im, X.Y. Chen, and G.C. Zha, "Detached Eddy Simulation of Stall Inception for a Full Annulus Transonic Rotor." Journal of Propulsion and Power, to appear.

[32] H. Im, X. Chen, and G. Zha, "Detached Eddy Simulation of Unsteady Stall Flows of a Full Annulus Transonic Rotor." ASME GT2010-23465, 2010.

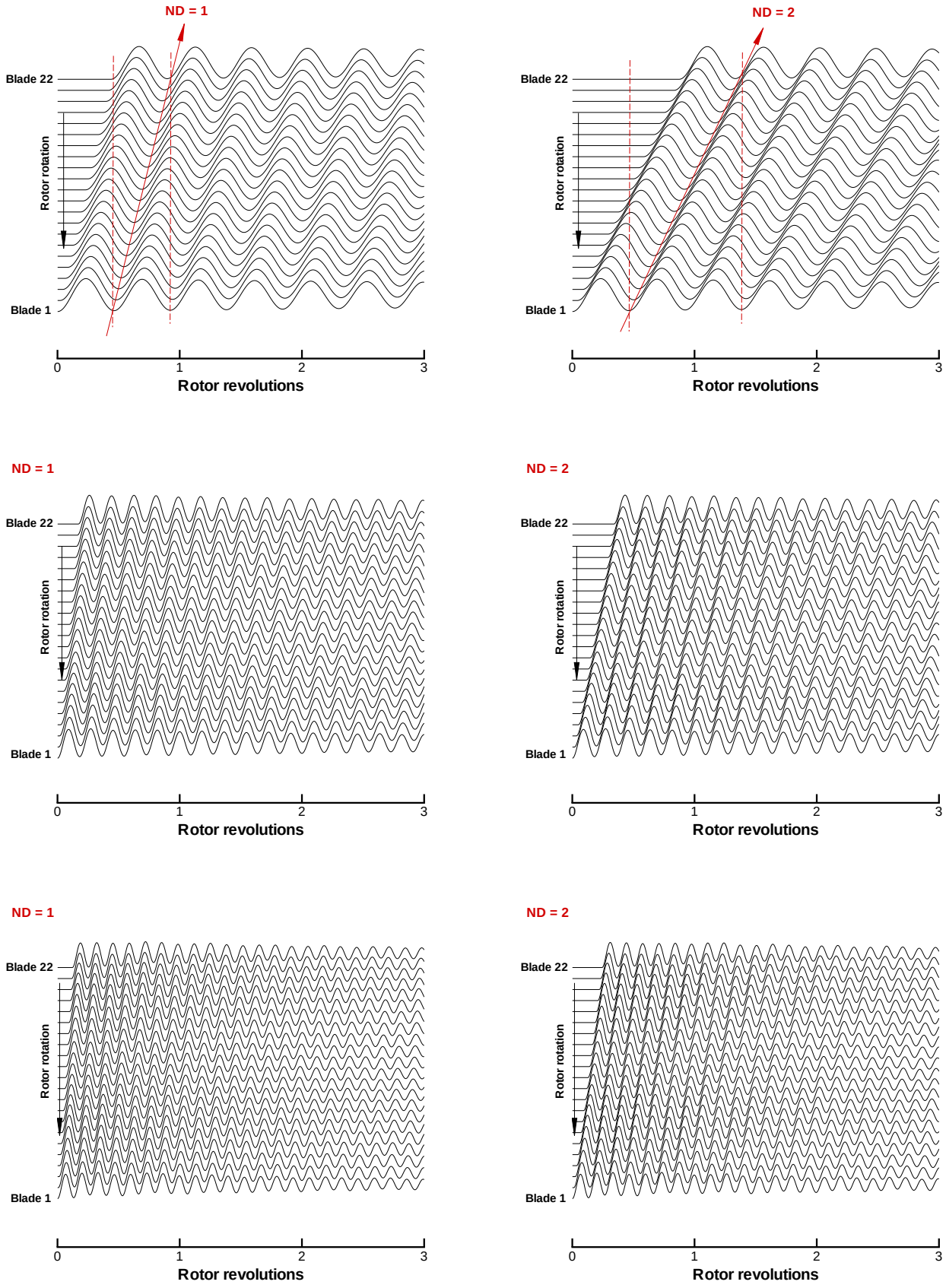

Figure 6: Modal displacements of NASA Rotor 67 with backward traveling wave; 1st mode of $N_D = 1$ (top left), 1st mode of $N_D = 2$ (top right), 2nd mode of $N_D = 1$ (middle left), 2nd mode of $N_D = 2$ (middle right), 3rd mode of $N_D = 1$ (bottom left), 3rd mode of $N_D = 2$ (bottom right)

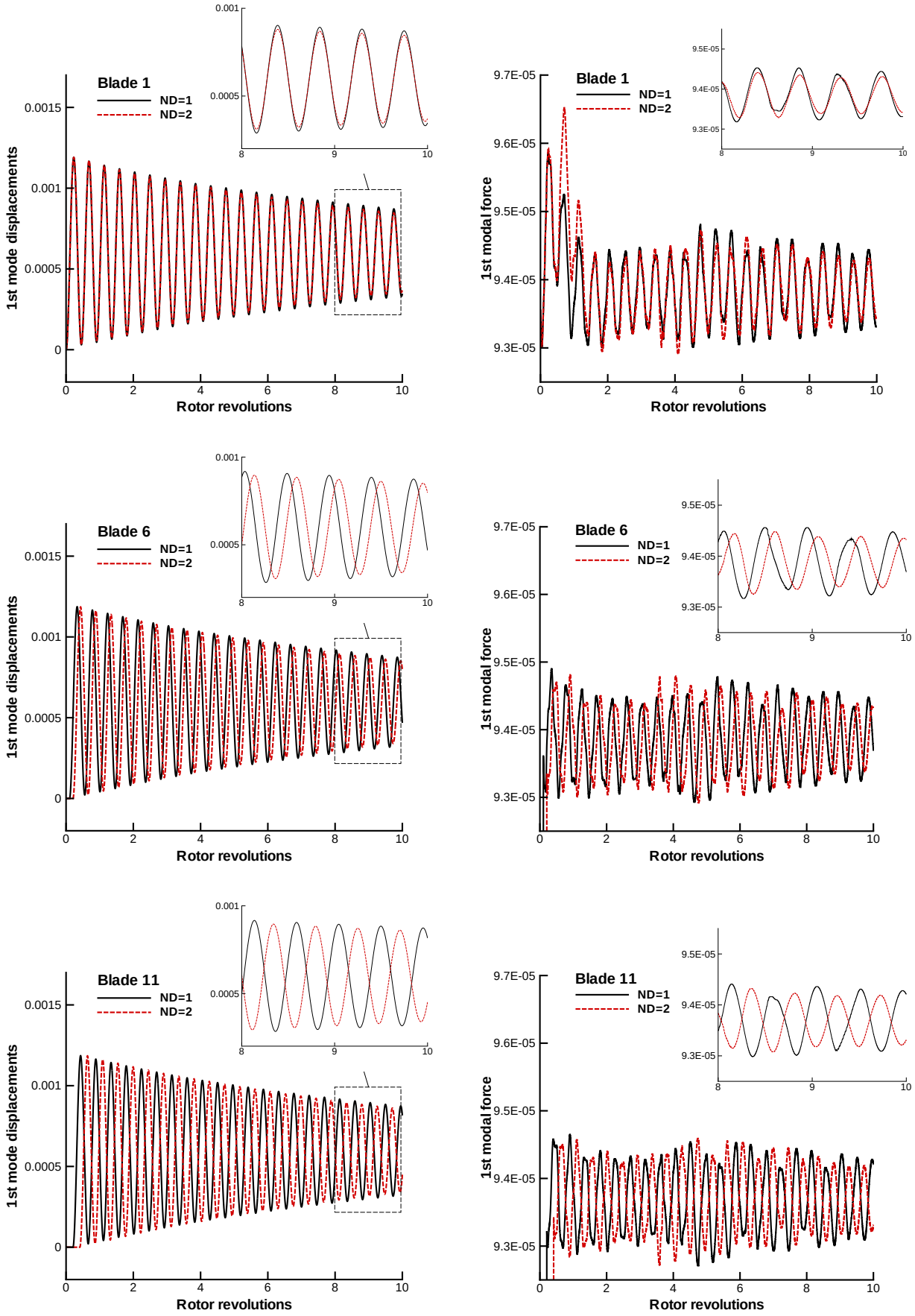

Figure 7: Dimensionless 1st modal displacements and force ($\frac{\tilde{\phi}_1^{*T}}{m_1^*} \cdot \mathbf{F}^* \cdot {V_f}^2 \cdot \frac{b_{\frac{3}{4}}^2 L}{V} \cdot \bar{m}$) of blade 1, 6 and 11

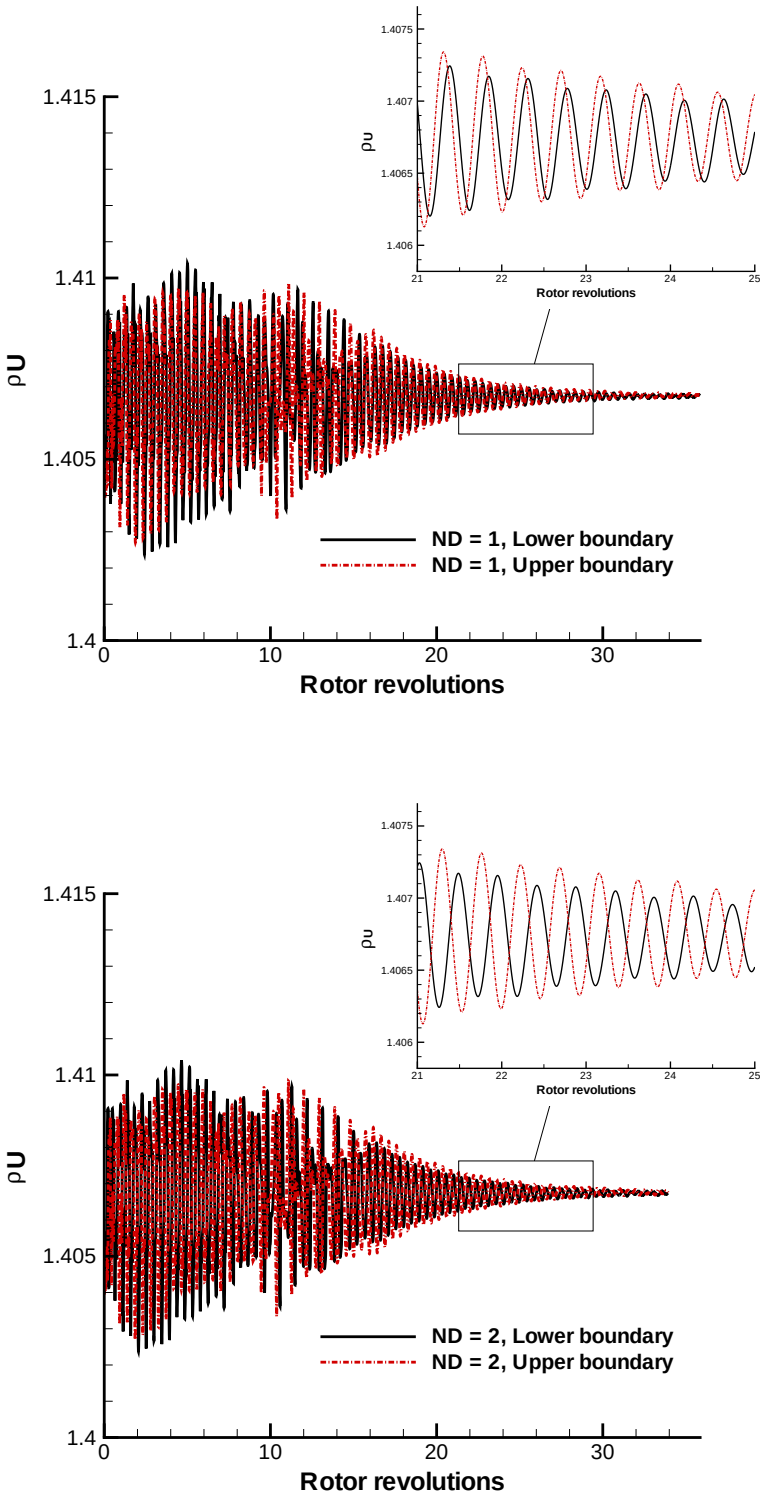

Figure 8: Comparison of normalized mass flux (ρU) at a upper/lower ghost cell boundary points for $N_D = 1$ and 2 predicted by the TSPL BC with single passage FSI

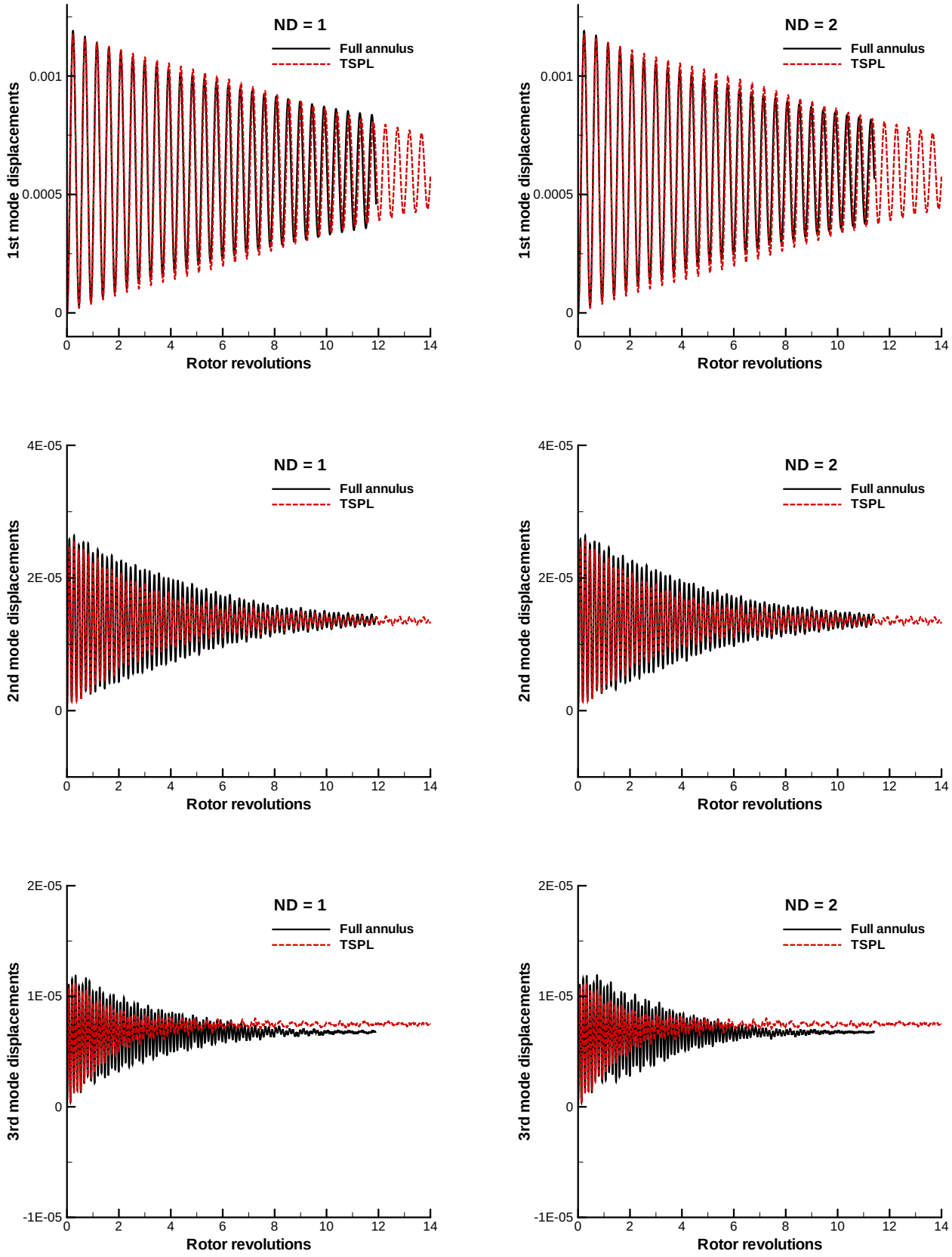

Figure 9: Modal displacements of NASA Rotor 67 predicted by the single passage with the TSPL BC and the full annulus for $N_D = 1$ and 2; 1st mode (top), 2nd mode (middle), 3rd mode (bottom)

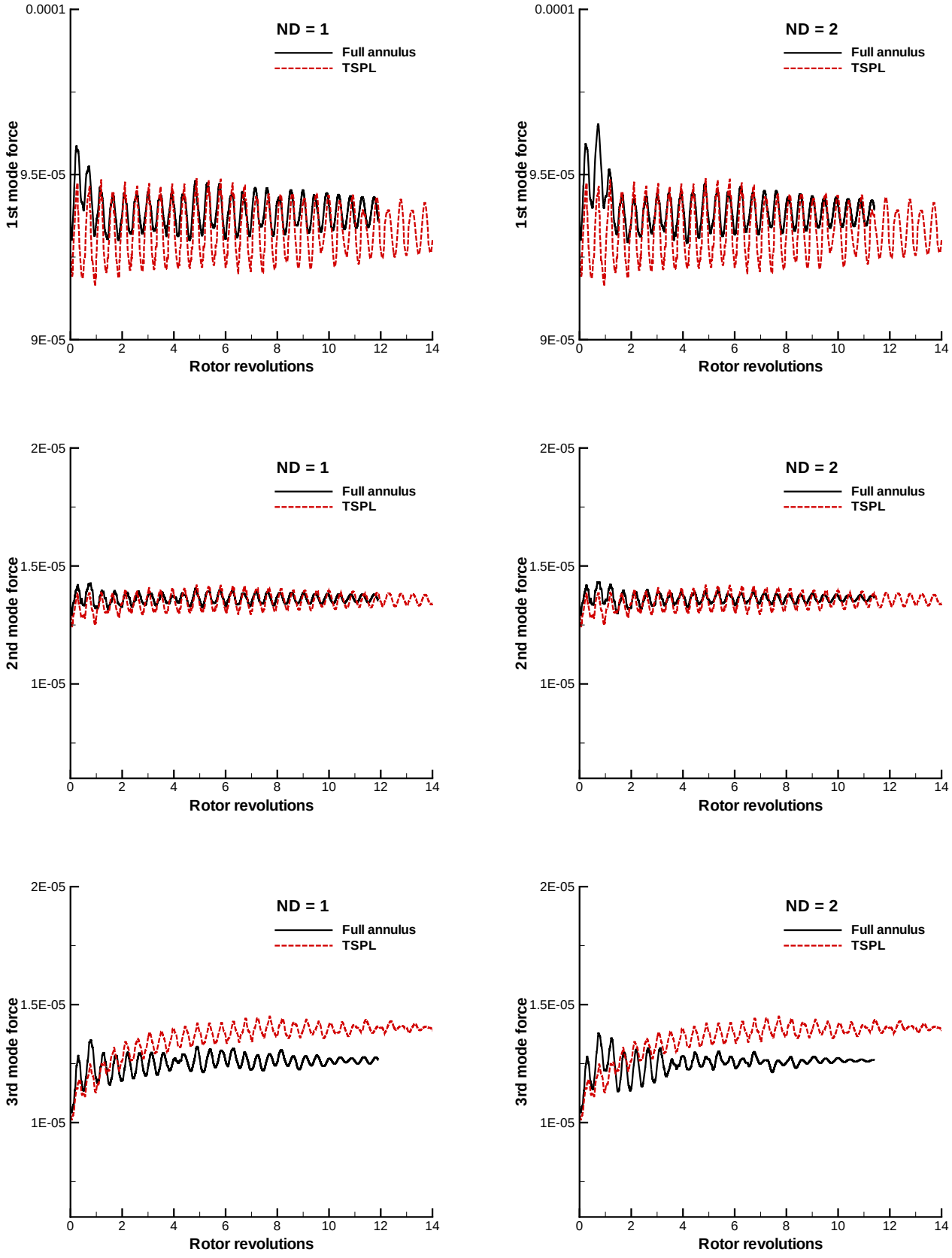

Figure 10: Modal force ($\frac{\tilde{\phi}_j^{*T}}{m_j^*} \cdot \mathbf{F}^* \cdot {V_f}^2 \cdot \frac{b_s^2 L}{\bar{V}} \cdot \bar{m}$) of NASA Rotor 67 predicted by the single passage with the TSPL BC and the full annulus for $N_D = 1$ and 2; 1st mode (top), 2nd mode (middle), 3rd mode (bottom)

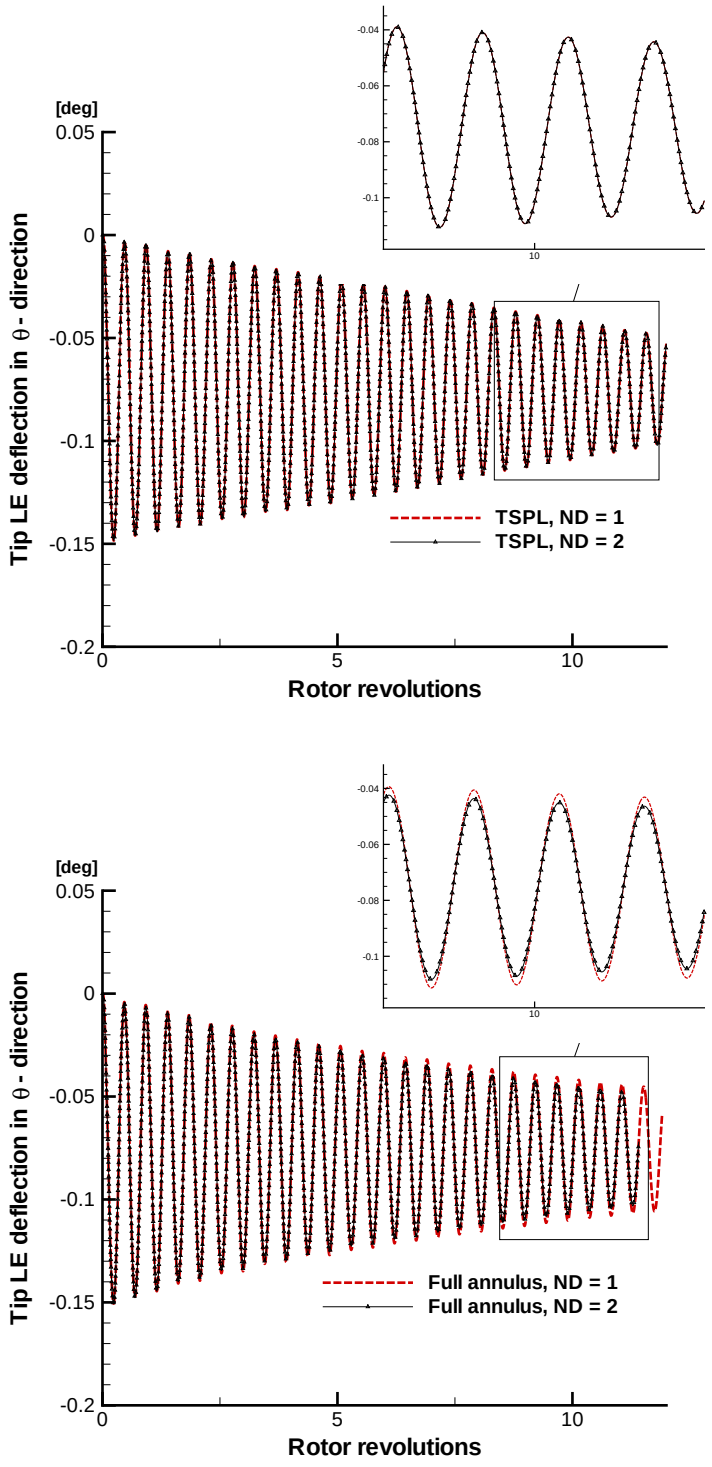

Figure 11: Blade 1 tip leading edge deflection in θ-direction for $N_D = 1$ and 2 predicted by the single passage with the TSPL BC and the full annulus; TSPL (top), full annulus (bottom)

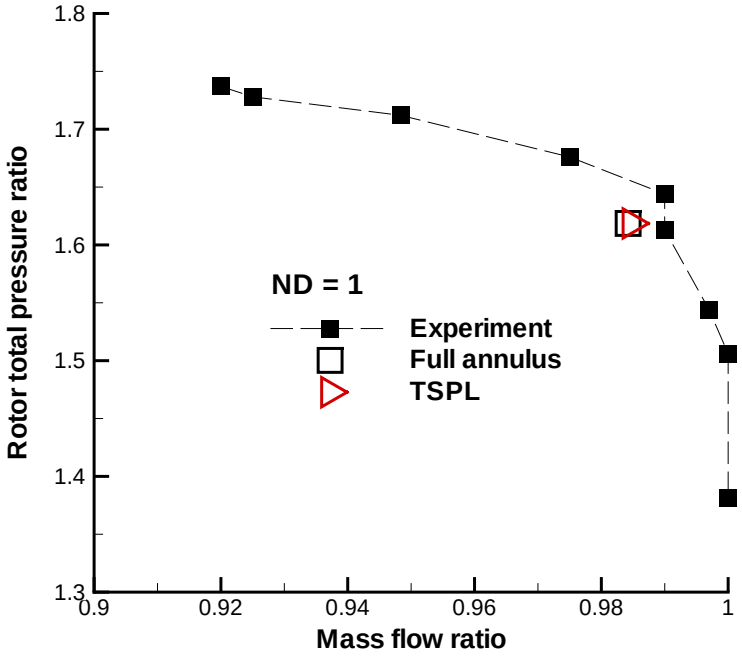

Figure 12: Predicted speed line at near peak